INORGANIC CHEMISTRY
FRONTIERS

RESEARCH ARTICLE

View Article Online
View Journal

Cite this: DOI: 10.1039/d5qi00870k

Peptide-mediated Al(III) (oxy)(hydr)oxide formation: the specific stages of phase separation for additive interactions matter†

Miodrag J. Lukić, *[a,b] Nele Marquardt,[b] Tim Schmalz [a,c] and Denis Gebauer *[b]

Received 29th March 2025,
Accepted 2nd June 2025

DOI: 10.1039/d5qi00870k

rsc.li/frontiers-inorganic

We demonstrate how Al(III) interactions with a 'biomimetic' model homo-peptide, polyaspartic (pAsp), with a narrow size distribution (around 20 amino acid monomer units), can lead to substantially different outcomes by governing Al(III) hydrolysis/phase separation. The addition of unhydrolysed Al(III) in aqueous peptide solutions results in dominant pAsp20 destabilisation and precipitation from the solution, failing to induce effective Al(III)(oxy)(hydr)oxide formation. Allowing the peptide-free Al(III) system to reach specific hydrolysis/phase separation stages, *i.e.*, just before and slightly after liquid–liquid phase separation, partly dissipating its chemical energy, followed by controlled peptide addition, leads to the formation of respective Al(III)(oxy)(hydr)oxide-peptide hybrids with smaller particles, higher Al(III) content, and well-preserved chemical properties of the peptide. This constitutes a *hydrolysis "spin-off"* strategy that exploits Al(III)–peptide interactions in distinct hydrolytic precursors, an approach transferable to multiple metals and polymeric systems. The reaction energetics determined by revisited isothermal titration calorimetry assays reflect an Al(III) hydrolysis "footprint" and its role in metal–peptide interactions. These insights are important for various applications of aluminium species, from vaccine adjuvants and related toxicity to enhancements of corrosion resistance.

Introduction

Interactions between Al(III) species and organic molecules are critical in pharmacy, medicine, sustainable energy, environmental protection, and hybrid materials. Adverse effects related to Al(III) in physiological or geochemical environments are consistently reported,[1,2] *e.g.*, structural destabilisation of biomolecules, salting-out effects, or cross-linking-induced precipitation. In this context, various questions regarding favourable interaction sites of Al(III) ions with polypeptides, *i.e.*, within the backbone, causing irreversible protein denaturation,[3] or with side-chain functions,[4] raise particular interest. Aspartic (Asp) amino acid residues are often involved in protein-metal binding, a process that affects the structural stability of proteins[5] and may lead to impaired chemical functionality.[6] Furthermore, the practical usefulness of metal-amino acid/peptide interactions has been demonstrated, *e.g.*, Asp-enhanced corrosion resistance of aluminium and its alloys[7] and stabilisation of adjuvants in alum-based vaccine formulations.[8] Also, peptides/proteins were successfully applied as additives for directing nucleation and crystallisation processes of different mineral systems.[9,10] For example, bovine serum albumin was reported to transform "Al_{13}"- and "Al_{30}"-mer poly-oxo-cations into amorphous $Al(OH)_3$ in a dose-dependent manner,[11] and the binding to Al(III) depends on the size and amino acid sequence of the polypeptides.[12] Organic molecules were used to alter Al(III) solubility and prevent potential toxicity,[13] to trap specific Al(III)$(OH)_x$ species,[14] and for the targeted synthesis of solid compounds.[15]

Al(III) hydrolysis is a spontaneous reaction occurring *via* numerous chemical/energetic states and polymerisation-condensation events, from monomers, oligomers, and prenucleation clusters, to polymers, ultimately leading to Al(III) (oxy)(hydr)oxide formation, given that the amount of substance, temperature, and pH are favourable. Al(III) (oxy)(hydr)oxide nucleation is inherently related to the hydrolysis process. Considering an acidic system, as the hydrolysis reaction proceeds from monomeric octahedrally-coordinated $[Al(H_2O)_6]^{3+}$ over $[Al(H_2O)_{6-x}(OH)_x]^{3-x}$ to the final Al(III) (oxy)(hydr)oxide phase, the overall reactivity changes due to the exclusion/rearrangement of hydration water molecules, hydroxyl groups

[a]Institute of Inorganic Chemistry, Leibniz University Hannover, Germany. E-mail: gebauer@acc.uni-hannover.de, miodrag.lukic@vin.bg.ac.rs
[b]Laboratory of Physics, "Vinča" Institute of Nuclear Sciences, National Institute of the Republic of Serbia, University of Belgrade, Serbia
[c]Institute of Radioecology and Radiation Protection (IRS), Leibniz University Hannover, Germany

† Electronic supplementary information (ESI) available. See DOI: https://doi.org/10.1039/d5qi00870k

and/or protons. Recently, it has been shown that chemical changes from olated to oxolated species trigger liquid–liquid phase separation in the Al(III) system under mildly acidic conditions.[16] Moreover, that work indicated the formation of oxolated species like Keggin Al_{13} only after phase separation, while monomeric and olation (prenucleation) cluster Al(III) species coexist in the prenucleation stage. Those oxolated species may serve as direct precursors of amorphous aluminium (oxy)(hydr)oxides as they lie closer in energy to the eventually forming solid than to monomeric and olation species.[17] On the other hand, mineral/organic/water interfaces are important for the final material's characteristics, *e.g.*, in catalysis[18] or CO_2 fixation,[19] and, evidently, also play a major role towards controlling nucleation and crystallisation. Thus, we hypothesise that by precisely controlling the hydrolytic chemistry of Al(III) and, with it, the stage of phase separation at well-defined points, the interactions between respective Al(III) species and organic molecules, *e.g.*, polymers, peptides or proteins, differ fundamentally. This would lead to distinct pathways towards Al(III) (oxy)(hydr)oxide nucleation, but also decisively determine the reaction outcomes in corresponding soil, aquatic, physiological and medical systems, where, *e.g.*, Al(III) toxicity is directly related to hydrolysis and speciation.[20,21] Moreover, corresponding insights will help to understand entangled and implicitly related processes of Al(III) hydrolysis and the interactions of these hydrolytic species with organic components in dynamic chemical systems. In this study, in order to simplify the inherently complex system, we focus on a defined model peptide additive for Al(III) hydrolysis, consisting of 20 aspartic acid monomers (pAsp20). This allows us to establish the fundamental roles of Al(III) hydrolysis/peptide interactions that, in turn, govern the reaction outcome. Understanding this behavior is a fundamental pre-requisite for studying distinct additive chemistries (*e.g.*, the effects of other side chain or backbone chemistries) in future work.

Indeed, our systematic and quantitative study of the interaction of Al(III) and pAsp20 homo-peptides at mildly acidic to neutral conditions using potentiometric pH-constant titrations as a methodological basis reveals distinct reaction outcomes by governing Al(III) hydrolysis and phase separation towards Al(III) (oxy)(hydr)oxide formation. Adding unhydrolysed Al(III) into a peptide solution (here labeled as Approach I, in brief, App. I), which is widely employed for assessing the effects of additives on the early stages of mineral precipitation, dominantly destabilises pAsp20, causing its early precipitation. On the contrary, the second approach (here labeled as Approach II, in brief, App. II) employs the controlled addition of pAsp20 to Al(III) solutions carefully driven to specific hydrolysis/phase separation stages, *i.e.*, before (BPS) and after (APS) the onset of the liquid–liquid phase separation. It is important to note that herein, we follow definitions and notions introduced in the framework of the so-called pre-nucleation cluster (PNC) theory.[22] In brief, dynamic PNCs are considered solutes, which can turn into liquid nanodroplets due to internal chemical changes. In the case of metal (oxy)(hydr)oxides, it was shown that this chemical change correlates with a change from olation to oxolation bridging within clusters, rendering the post-nucleation oxolation clusters less dynamic than olation PNCs.[16,23] Previous works determined the characteristic points with respect to this phase separation mechanism in the titration experiments also employed here, allowing us to prepare well-defined APS and BPS states for interacting with pAsp20. App. II shows that even slight differences in Al(III) hydrolysis/phase separation stages consistently induce distinct types of interactions with pAsp20, revealing peptide-induced Al(III) (oxy)(hydr)oxide formation. This shows that governing metal chemistry to a specific chemical-hydrolysis-phase separation state, here denoted as a *hydrolysis "spin-off"* strategy, is a viable way for selecting distinct metal–peptide interactions and directing the reaction outcome. A revisited isothermal titration calorimetry (ITC) assay suitable for studying hydrolysing systems is developed, clearly reflecting a corresponding "hydrolysis footprint" in the metal–peptide interactions.

Results and discussion

The titration curves directly show the hydrolysis progress by titrating NaOH to counter the production of protons and maintain a constant pH level. At pH 4.5 following App. I, Fig. 1(A), the titration curve of the Al(III) system without pAsp20 exhibits an initial linear part followed by a transition towards a second linear region with stronger base consumption due to liquid–liquid phase separation, delineating, essentially, the pre-nucleation (first linear part) and post-nucleation (second linear part) regimes, as previously demonstrated elsewhere.[16] At pH 3.0 and 4.0, Fig. S1,† the reference Al(III) titration curves without pAsp20 show a very small amount of NaOH required to keep the pH constant, revealing a minor extent of Al(III) hydrolysis. At pH 5.0, the behavior is similar to that at pH 4.5, but the first linear part is significantly shorter due to a higher driving force towards Al(III) hydrolysis. In the presence of pAsp20, the Al(III) system exhibits a rather distinct behaviour, *i.e.*, the addition of unhydrolysed acidic Al(III) solution into 0.15 g L^{-1} peptide solutions induces an immediate increase in base consumption reflected in c_{ex}(NaOH), Fig. 1(A). This is accompanied by a strong decrease in the solution transparency due to occurring precipitation. After the strong initial increase in base consumption, the slope of the titration curve becomes similar but slightly lower than the one of the reference Al(III) system. This indicates that the effect of pAsp20 is practically exhausted at very low $c_{added}(Al^{3+})$. Subtracting the titration curve of the reference Al(III) system from that with pAsp20, Fig. S2,† reveals that after the initial period (when the presence of pAsp20 dominates the chemical behaviour), Al(III) hydrolysis is slightly suppressed. This can be explained by the secondary nucleation of Al(III) (oxy)(hydr)oxide on Al(III)–peptide precipitates. Consistently, qualitatively the same behaviour occurs when the pAsp20 concentration is changed, Fig. S3;† however, the changes are limited to the initial part of the titration curves. The $c_{added}(Al^{3+})$ required to induce precipitation systematically increases with increasing pAsp20 concentration,

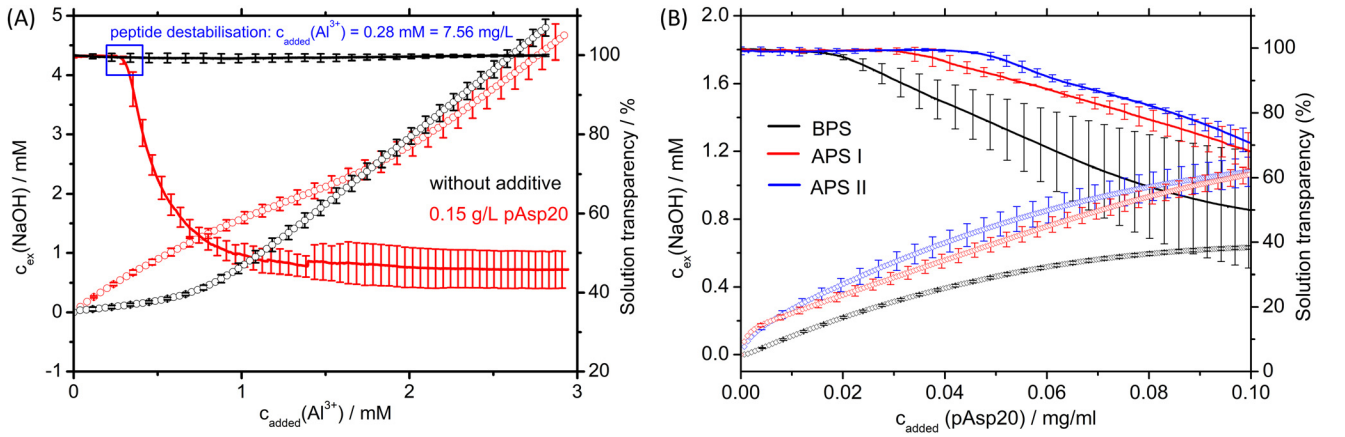

Fig. 1 Titration curves (empty symbols) obtained in (A) App. I by dosing acidic Al(III) into peptide solution at pH 4.5, and (B) App. II by dosing a 0.5 mg mL^{-1} solution of pAsp20 (solution pH adjusted to 4.5) into Al(III) solutions in BPS and APS I and II (ESI, Fig. S5†) states at pH 4.5. The left axis of each plot shows the concentration of NaOH added to keep the pH value constant (corrected for the NaOH added to neutralise the addition of the acidic Al(III) solution), c_{ex} (NaOH). Thus, the titration curve accounts only for the Al(III) hydrolysis and the interaction with pAsp20. The right y-axes show the corresponding solution transparency (solid lines). Drops in the solution transparency curves represent increasing turbidity as measured by an optrode at 610 nm.

while the drop in solution transparency becomes stronger. This shows that the amount of precipitate predominantly correlates with the amount of pAsp20. However, $c_{added}(Al^{3+})$, at which precipitation occurs, is very low. Equivalent experiments at pH 3.0 show correspondingly weaker interactions with pAsp20 than at higher pH values, but the interaction becomes again stronger as $c_{added}(Al^{3+})$ increases, Fig. S1.† This occurs at pH 4.0 and 5.0, pAsp20 precipitates at low $c_{added}(Al^{3+})$ as well. However, the behavior at pH 5.0 is more similar to that at pH 4.5 (*i.e.*, strong hydrolysis driving force) than at pH 4.0.

In App. II, pH-constant titrations of the Al(III) system without peptide were performed at pH 4.5 to reach carefully selected hydrolysis/phase separation states, Fig. S4.† Then, the titration was stopped, and immediately (<10 s) afterwards, the pAsp20 solution was continuously dosed into the as-prepared Al(III) solution state. The absolute differences in $c_{added}[Al^{3+}]$ among the different investigated hydrolysis/phase separation are very little and are usually exceeded in experimental studies involving the Al(III)–organic interactions,[24] although they represent distinct chemical and structural characteristics of Al(III) hydrolytic species.

The selected BPS state is characterized by the presence of monomeric Al(III) in equilibrium with Al(III) pre-nucleation clusters (PNC) species, which, in the case of the hydrolysing/condensating systems, correspond to olation oligomers, while in the APS states, tetrahedrally coordinated Al_{13} Keggin species may emerge alongside these Al(III) species, as shown previously for the Al(III) system.[16,23] Remarkably, no precipitate formation is detectable in any of these states, *i.e.*, the solutions remain transparent, at least, before pAsp20 addition. Indeed, the titration curves for App. II, Fig. 1(B), illustrate different behaviour than for App. I, where the polymer is present from the beginning. Continuous dosing of pAsp20 solution into the BPS state of the Al(III) system induces a monotonous increase in the base consumption required to keep the pH constant. However, unlike in App. I, this does not cause a sudden drop in the solution transparency. Rather, the pAsp20 concentration, at which the solution starts to become turbid (as measured by an optrode at 610 nm) increases from the BPS to APS II states with increasing total Al(III) concentration. When the APS states of the Al(III) system are probed, the distinct behaviour becomes more evident: the initial base consumption to keep the pH constant is way higher than for the BPS state, indicating qualitatively and quantitatively different interactions. After stopping the Al(III) addition in the APS II state, Al(III) hydrolysis proceeds (*i.e.*, continues to produce protons) (Fig. S5,† the red curve). This process is compensated by NaOH addition to keep the pH constant, until reaching an equilibrium state where the pH remains constant. Indeed, the initial development of the corresponding APS II titration curve with pAsp20, Fig. S5† (the black curve), is dominated by the hydrolysis behavior as observed for the pure Al(III) after phase separation. Remarkably, the interactions with pAsp20 effectively suppress Al(III) hydrolysis by binding Al(III) hydrolytic species, keeping it below the hydrolysis level of the pure APS II system (the green dashed line) almost up to >4 hours (15.000 s). After the initial, hydrolysis-dominated behaviour, Al(III)–peptide interactions become dominant, giving rise to the characteristic final development of the titration curves. Thus, by selecting an appropriate hydrolysis/phase separation state in App. II, specific reaction states in the Al(III) system are accessible for interactions with the peptide, which is not possible in App. I, where initially formed Al(III) hydrolytic species are immediately exposed to interaction with pAsp20.

Significant spectral changes occur during precipitation in App. I in the presence of pAsp20 (the sampling points were selected according to the turbidity measurements in the titration experiments—in the initial, middle, and late precipitation

stages, Fig. S6†) until the final titration point was reached. FTIR spectra of pure pAsp20, solids derived from the titration experiments in App. I and App. II at pH 4.5 in the presence of pAsp20, and amorphous $Al(OH)_3$ (prepared at pH 7 and used as a reference) in the fingerprint region from 1800–400 cm^{-1} are shown in Fig. S7.† The corresponding full spectra, also at pH 4, 5 and 7, are provided in Fig. 2. The pure pAsp20 shows characteristic symmetric and asymmetric COO^- vibrations at 1389 and 1588 cm^{-1}, respectively. The amide I band occurs as a shoulder at 1645 cm^{-1} due to the overlap with the band due to COO^-. At higher wavenumbers, H-bonded N–H and CH_2 vibrations can be observed. Amorphous $Al(OH)_3$ exhibits broad bands, where the strongest band at 534 cm^{-1} originates from Al–O bonds of octahedrally coordinated Al(III), while the low-intensity band at 851 cm^{-1} can be assigned to the Al–O bond of tetrahedrally-coordinated Al(III). In the wavenumber range of approximately 870–1150 cm^{-1}, a broad feature appears, which originates from Al–O–H and AlO–OH vibrations.[25,26] In the region of 1250–1700 cm^{-1}, several broad, middle-intensity bands appear, originating from H–O–H vibrations, whilst the very broad band in the range of 3000–3600 cm^{-1} represents the O–H vibrational region, Fig. 2.

In the solids obtained at pH 4.5, the strongest change along the distinct stages probed occurs for the symmetric COO^- vibration, accompanied by smaller changes in the corresponding asymmetric mode (Fig. S7†). The symmetric COO^- band splits into two bands and shifts from 1389cm^{-1} to 1406 cm^{-1} and 1456 cm^{-1}, indicating the formation of more rigid bonds, possibly due to the formation of bridging or bidentate (mononuclear) complexes. The intensities of the newly developing bands decrease from the initial to the final solid upon continuing precipitation and further Al(III) addition. Whilst the one at 1456 cm^{-1} exhibits a stronger gradual decrease, these bands also shift back slightly towards lower wavenumbers (from 1406 cm^{-1} and 1456 cm^{-1} to 1404 cm^{-1} and 1451 cm^{-1}, respectively). Simultaneously, the Al–O region shows two characteristic bands at 659 cm^{-1} and 572 cm^{-1}. The former band retains the initial position and similar intensity during the entire precipitation process, suggesting that it represents the initial formation of Al–O bonds with the oxygen atom from carboxylate groups of the peptide. The latter band shifts to 558 cm^{-1} upon further Al(III) addition, *i.e.*, moving towards a position characteristic for Al–O bonds within octahedrally coordinated Al(III) sites. Its intensity constantly increases, implying possible secondary nucleation of Al(III) (oxy)(hydr)oxide, as already mentioned in the context of the titration date above. The above-discussed spectral changes in the carboxylate region thus relate to the dynamic and continuous development of Al–O bonds within octahedrally-coordinated Al(III). The amide I band at 1645 cm^{-1} in all solids derived from App. I overlaps with the broad vibrational bands in the spectral region around 1600 cm^{-1}, suggesting that the amide I backbone region, besides the carboxylate group, is possibly involved in the interaction with Al(III) species. This can be understood as a consequence of the backbone proximity since only one $-CH_2$ group is in the sidechain. The OH region (3000–3700 cm^{-1}), upon continuing precipitation, remains more similar to that of pAsp20 than to that of $Al(OH)_3$, Fig. 2. Remarkably, almost no bands develop in the Al–O–H region (870–1150 cm^{-1}) in App. I. Increasing the pAsp20 concentration in App. I, no further spectral characteristics of Al(III) (oxy)(hydr)oxide appear, Fig. S8,† which agrees with the results from the titration curves and an exhaustion of the additive effect after the initial reaction between Al(III) and the peptide.

In App. II at pH 4.5, dosing pAsp20 solution into pre-hydrolysed Al(III) states induces distinct spectral features compared to App. I (Fig. 2 and Fig. S7†). The extent of the shift of the symmetric COO^- vibrational band towards higher wavenumbers is lower than in App. I, implying that less rigid bonds to Al(III) are formed. The solid derived from the BPS state in App. II exhibits FTIR spectral characteristics that are qualitatively similar to those of the final solid in App. I, although the amount of added Al(III) in the former approach is way lower than in the latter (for more details, please see ESI, section 1.1†). In case of the APS I and II hydrolysis/phase separation states, upon dosing the pAsp20 solution, the symmetric COO^- vibrational band changes to a lesser extent and remains closer to the positions of the bands of pure pAsp20. Also, the intensity of the newly formed band decreases. The most significant difference occurs in the region of 800–1100 cm^{-1}. For the

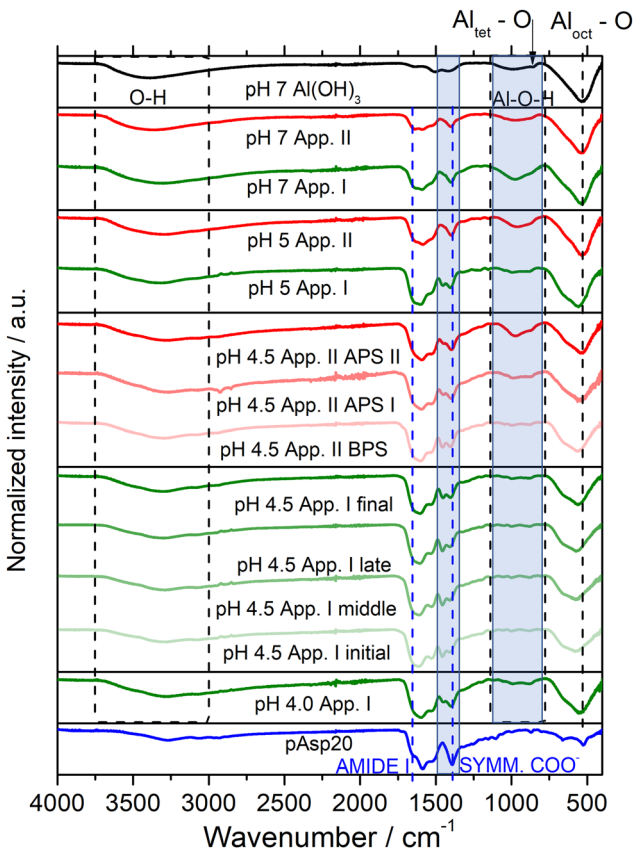

Fig. 2 FTIR spectra of solids derived from titration experiments following App. I and App. II.

solids derived from APS I and II, this spectral region is similar to that of $Al(OH)_3$ obtained at pH 7. Regarding the Al–O vibrations of octahedrally-coordinated Al, the band at 653 cm^{-1} does not change its position and intensity, whilst the band at 550 cm^{-1} shifts to lower wavenumbers (532 cm^{-1}). This is practically identical to the corresponding band in $Al(OH)_3$, implying similar chemical bonding. The amide I band becomes better distinguishable when compared to App. I as the system develops towards APS II. The spectral region of the O–H stretching vibration at higher wavenumbers progressively develops from the BPS to the APS II stage. The developed vibrational bands indicate the formation of a mixture of Al(III) (oxy)(hydr)oxide and hydroxide, probably gibbsite.

At pH 5, in App. I, the band due to the symmetric carboxylate vibration splits, whilst it is practically preserved in App. II. The broad feature in the OH region at high wavenumbers is better developed than at pH 4.5, in line with the aqueous Al(III) chemistry, as $Al(OH)_3$ formation is more favourable at pH 5. In App. II, the same region essentially resembles that of $Al(OH)_3$. Comparing the two approaches further, the amide I region in the presence of pAsp20 in App. II can be better distinguished than in App. I. The band due to Al–O vibrational modes at lower wavenumbers becomes more uniform and the shoulder at higher wavenumbers is weaker in solids from App. II than App. I. The intensity of bands in the Al–O region in App. II increases compared to App. I (relative to the intensities of bands in the fingerprint region for the pristine additive). At pH 7, both approaches provide clear evidence for the formation of $Al(OH)_3$–pAsp20 hybrids, Fig. 2, whilst the bands in the pAsp20 region exhibit lower relative intensities than at lower pH values, implying favourable $Al(OH)_3$ formation. Altogether, the possibility to tailor chemical interactions in the different systems based on the extent of hydrolysis/phase separation and the addition sequence of the reactants is obvious.

The particles derived in App. I at pH 4.5 in presence of pAsp20, Fig. 3(A), are mostly irregular and heterogeneous, with a size around 200 nm. Smaller particles also appear, implying, possibly, two different growth mechanisms. Increasing the pAsp20 concentration leads to bigger but also more irregular particles, Fig. 3(B). In App. II, the particles are way smaller, between 50 and 100 nm, and exhibit a rather high uniformity in size and shape in both BPS and APS II states, Fig. 3(C and D). This implies that more controlled nucleation and growth conditions are realized in presence of the peptide in these hydrolysis stages. $Al(OH)_3$ synthesized at pH 7, Fig. 3(E), exhibits uniform particles below 100 nm, which are morphologically similar to the particles derived in App. II.

The thermogravimetric (TG) behaviour of the solids formed in the different Al(III) systems with pAsp20, Fig. 3(G), shows an initial mass loss of about 10–15 wt% up to 110 °C, originating from loosely bound water. The main step of mass loss is the degradation of the organic constituents, accompanied by an exothermic feature in the DSC trace. The mass loss due to decomposition of the organics is very sensitive to the chosen experimental approach. In App. I, the pAsp20 degradation occurs at 375 °C, in the BPS state, at 378 °C, whilst in the APS states, the organics decompose at 390 °C, indicating improved thermal stability, which can be explained by the different binding characteristics discussed above. The remaining mass of the solid (in the form of Al_2O_3) after the thermal treatment is higher in App. II than in App. I (except for BPS due to the small amount of added Al(III)); the mass of the remaining solid increases from BPS to the APS III state, and in the latter equals 35%, which is significant compared to 58% for the pure $Al(OH)_3$, Fig. 3(F). Based on EDX analyses (spectra not shown), the amount of Al(III) increases in App. II as the hydrolysis/phase separation proceeds, becoming higher than in App. I. Here, this is quantified as the Al/N ratio, a relative measure of the Al(III) amount over the peptide amount in the solid, assuming that N originates dominantly from pAsp20. For example, for APS II, the Al/N ratio is ~1.75, and for the final solid from App. I, it is ~1.1. ICP-OES measurements of the remaining supernatant solution after removing the precipitate, Table S1,† show that Al(III) is more efficiently used in App. II than in App. I, which, altogether, corroborates the notion of a more controllable and adjustable reaction outcome when applying App. II. Although measurable turbidity was observed in the titration experiments in App. II at higher pAsp20 concentrations, Fig. 1, low-intensity spikes in the transparency curve sporadically appeared earlier. Nevertheless, upon stopping the peptide addition after 5000 s, *i.e.*, at a pAsp20 concentration of ~0.01 g l^{-1}, in the BPS and APS II states, where no macroscopically detectable drop in the solution transparency occurs as measured by an optrode at 610 nm, millimetre-sized, white flocs floating on the surface of the solution volume in the titration vessel of the APS II experiment appeared, Fig. 3(H). The whole reaction volume was isolated by vacuum filtration through a 50 nm filter (followed by washing with HCl at pH 4.5 and then MiliQ water). The isolated solids consist of small and uniform particles, Fig. 3(I and J), with a size of less than 50 nm; the EDX analysis indicates a significantly higher Al/N ratio than in the final solids (~4), Fig. 3(K), implying that these species represent intermediate species towards the final material. This is especially important for the Al(III) system and its interaction with the model peptide, pAsp20. While this is also expected for other peptides/polymers, Al(III) is different and more invasive compared to other triply charged metals, *e.g.*, Fe(III). Indeed, Fe(III) induces no precipitation of pAsp20 following App. I, but rather a controlled solid formation, Fig. S9.†

The energetics of the Al(III)–peptide additive interactions were assessed at different pH values using isothermal titration calorimetry (ITC), Fig. 4. In previous literature, 0.1 M NH_4-acetate buffer was applied during ITC measurements of Al(III) binding,[27] also in the neutral pH range, where it has a minor buffering capacity.[28] Alternatively, sodium acetate buffer was used to study the interaction of Ga(III) with a peptide.[29] Here, by applying potentiometric titration experiments equivalent to App. I in the presence of 0.1 M NH_4–acetate buffer, we observed strong interactions between Al(III) and the buffer (see below). To avoid this, ITC experiments without buffers were designed to complement the titration experiments to the

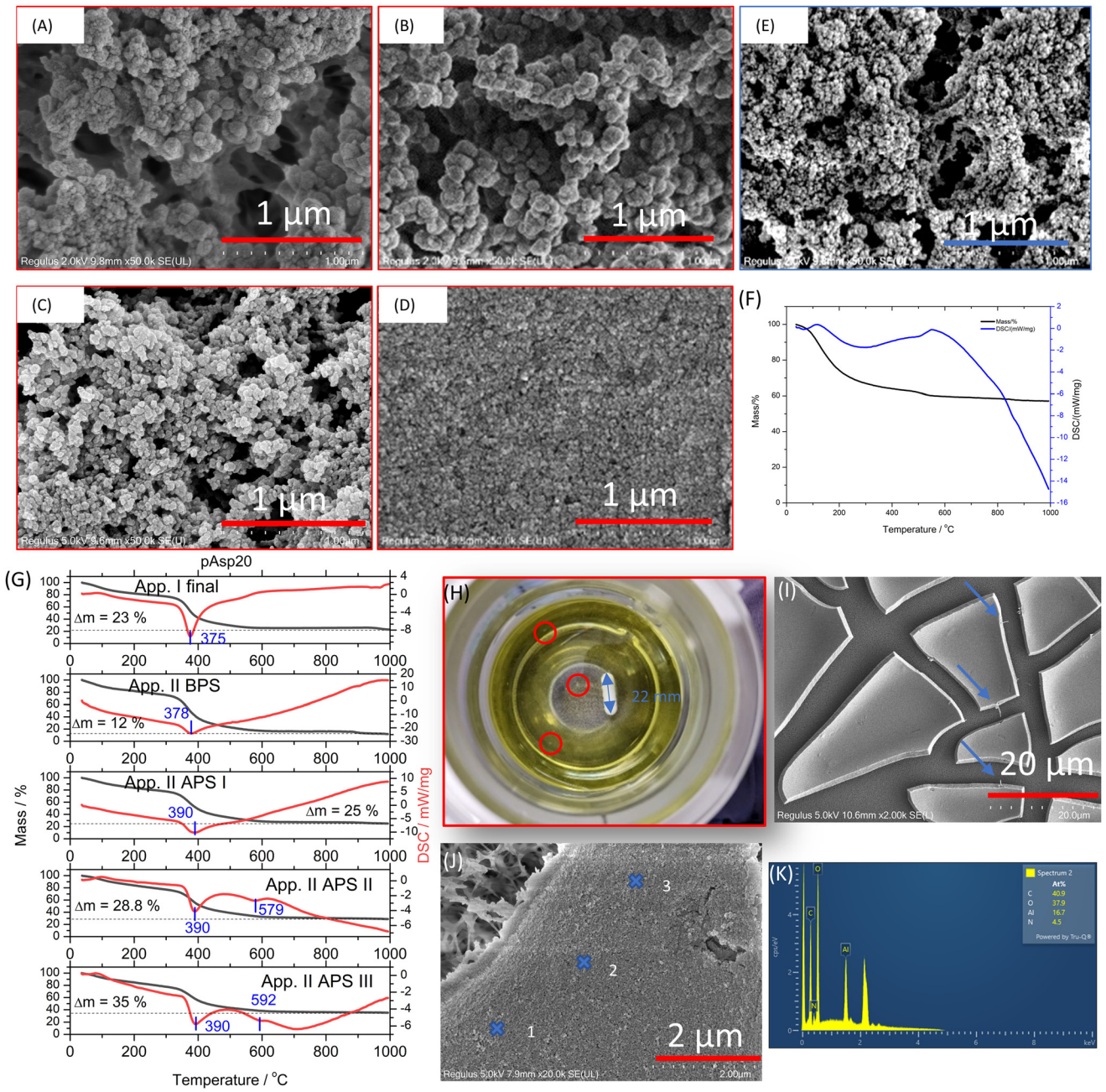

Fig. 3 SEM images of the solids derived at pH 4.5: (A) App. I 0.15 g L^{-1} pAsp20, (B) App. I 0.5 g L^{-1} pAsp20, (C) App. II BPS, (D) App. II APS II, (E) Al$(OH)_3$ pH7; the scale bar for these micrographs is 1 µm; (F) TG-DSC curve of Al$(OH)_3$ synthesized at pH 7 and (G) TG-DSC measurements up to 1000 °C in an 80%N_2/20%O_2 oxidative atmosphere of the solids derived from App. I and App. II titration experiments at pH 4.5; (H) photograph of the solution in the titration vessel after titrating for 5000 s the Al(III) APS II state using pAsp20 at pH 4.5 following App. II, showing millimetre-sized floating flocs highlighted by red circles. SEM images of the (I) BPS (dried blocks that consist of small particles) and (J) APS II states-derived intermediates after 5000 s; the scale bar in (I) is 20 µm, and in (J) is 2 µm; (K) EDX spectrum of spot 2 in (J).

highest possible degree. The pH of the dosed Al(III) solutions was lower (but not more than ~0.5–1.5 pH units, more information in ESI, section 1.3†) than the actual pH value in the ITC chamber. This ensures experimental conditions as in titration experiments in App. I, *i.e.*, dosing more acidic Al(III) solution into solutions at higher pH values, but without inducing strong pH changes (ΔpH < 0.05 pH unit). The ITC-signal intensity upon dosing pure 0.5 mM Al(III) into HCl (the bottom graphs in Fig. 4(A–D)) is low at pH 4.0 since Al(III) hydrolysis occurs to a minor extent. Consistently, it becomes significantly stronger (4–5 times) at pH 4.5 and 5. For dosing a buffered Al (III) solution in buffered pAsp20 at pH 4.5, following previously reported ITC procedures,[27] way weaker ITC-signal intensities are recorded, Fig. S10(A),† even at a two times higher Al(III)

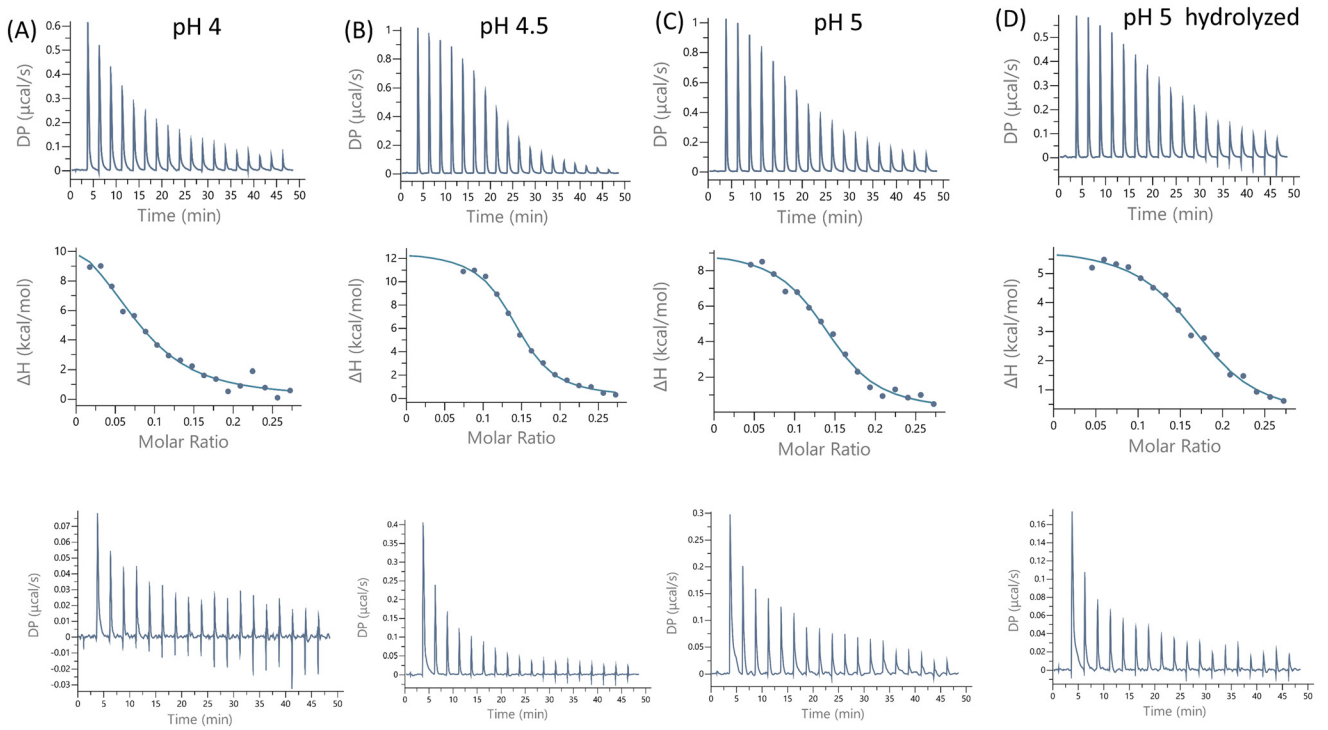

Fig. 4 ITC traces in the Al(III)–pAsp20 system at different pH values: (A) 4.0, (B) 4.5, (C) 5.0, and (D) 5.0 after forced hydrolysis. The bottom row of the panels represents the energetic effect originating only from dosing Al(III) in HCl at the given experimental conditions, demonstrating the effect of Al(III) hydrolysis (see also Fig. S11†).

concentration, compared to unbuffered systems. Indeed, if the buffered Al(III) solution is dosed in the buffer, as a control experiment, only pure dilution is explored in the buffered systems, Fig. S10(B).† Thus, in presence of the buffer, no actual insight into the Al(III) hydrolysis behaviour can be obtained, since Al(III) strongly interacts with the buffer, as is obvious from the titration experiment, Fig. S10(C).† Keeping in mind that these signals are used as a reference for the evaluation of the ITC results of the Al(III)–pAsp20 systems, neglecting to address the Al(III) hydrolysis in ITC data directly affects the results.

As the first experimental points are strongly influenced by Al(III) hydrolysis at pH 4.5 and higher, they are not considered in the data evaluation, and corresponding standard enthalpy ($\Delta H°$) values fall significantly below the s-shaped curve (as is understandable from the difference in absolute power (DP) values of the actual experiment and control experiment, in Fig. 4 the first and the third row). The thermodynamic and binding parameters are distinct for chemical environments with low (pH 4.0) and high (pH 4.5 and 5.0) driving forces for Al(III) hydrolysis. The interaction is spontaneous and entropy-driven. The reaction becomes more favourable at higher pH values, *i.e.*, the standard free enthalpy ($\Delta G°$) becomes more negative, Table 1; the enthalpic and entropic contributions significantly increase at pH 4.5 compared to 4.0, whilst at pH 5.0, the enthalpic term is less limiting. Driving Al(III) hydrolysis by adding NaOH solution before conducting an experiment at pH 5.0 (the system starts to buffer the pH change at pH ~4.7) leads to a higher stoichiometry (*i.e.*, the number of Al bound per COOH group) but significantly decreases the enthalpic and entropic contributions. Consistently, already hydrolysed Al(III) solution exhibits less energetic changes upon subsequent

Table 1 Thermodynamic and binding parameters, with standard deviations, of the Al(II)–pAsp20 system derived from ITC measurements at 25 °C (N = 3)

System	pH	n*	$K_D/10^{-6}$ M	$\Delta H°$/kJ mol^{-1}	$\Delta G°$/kJ mol^{-1}	$\Delta S°$/J mol^{-1} K^{-1}
Al-pAsp20	4.0	0.081 ± 0.005	7.20 ± 1.86	49.79 ± 4.60	−29.46 ± 0.63	265.23 ± 13.33
Al-pAsp20	4.5	0.144 ± 0.005	1.61 ± 0.02	55.09 ± 2.05	−33.08 ± 0.30	295.63 ± 0.83
Al-pAsp20	5.0	0.137 ± 0.005	3.67 ± 1.36	41.09 ± 4.02	−31.13 ± 0.96	242.07 ± 10.95
Al-pAsp20 (hydrolysed)	5.0	0.175 ± 0.004	4.05 ± 0.91	27.40 ± 2.43	−30.84 ± 0.63	195.48 ± 6.60
Al-pAsp20$_{buff}$	4.5	0.113 ± 0.008	14.75 ± 0.35	18.53 ± 0.67	−27.57 ± 0.06	155.06 ± 0.99

* Stoichiometry (the number of Al bound per COOH group).

dosing into the peptide solution when compared to the ITC experiments at pH 5.0. The binding constant does not show a clear trend with changing pH, but seems to be way lower at pH 4.5 than at other pH values. As expected, the interaction energetics in the presence of a 0.1 M NH_4–acetate buffer are completely different and strongly underestimated, as determined at pH 4.5, caused by the binding of Al(III) to the buffer molecules. It should be noted that emulating the App. II titration experiments in ITC, *i.e.*, dosing 0.5 mg ml^{-1} pAsp20 solution into Al(III) in the APS II state at pH 4.5, did not produce data that could be evaluated (not shown here); no saturation of the ITC-intensity occurs and the reaction produces a lower DP signature, implying a different interaction mechanism. At pH 3, no measurable heat profiles due to binding of Al(III) and pAsp20 were detected at the used reactant concentrations at 25 °C.

The present study indicates the relevance of Al(III) hydrolysis and phase separation for the outcome of metal–peptide interactions. In a peptide-containing system, the addition of unhydrolysed Al(III) species causes the metal hydrolysis and the interaction of hydrolysed metal species with the peptide, the balance of which is the clue towards favourable reaction pathways. Fig. 5 schematically illustrates the two different implemented approaches, proposing corresponding interaction mechanisms. According to our results, dosing unhydrolysed Al(III) into peptide solutions (App. I) primarily leads to the precipitation of pAsp20, probably as cross-linked Al(III)-salts, partly deteriorating the peptide. In App. I, any dosed Al(III) species, after being subjected to sudden hydrolysis due to the higher pH in the pAsp20 solution, interacts with the available COOH groups of pAsp20. Monomeric or oligomeric Al(III) species, *e.g.*, Al(III) PNCs, can interact with COOH groups from distinct pAsp20 chains, leading to their irreversible cross-linking and removal of water molecules from the hydration layer of the peptide. This finally leads to the peptide precipitation from the solution at a sufficiently high Al(III) concentration. By using App. II, we allow the system to reach distinct hydrolysis/phase separation states. In this way, the system partly reacts along the hydrolysis pathway, decreasing its interaction potential with the peptide *via* oligomerisation and formation of Al–O(H)–Al or Al–O–Al bonds. This can occur either at the same or different pH values. Then, pAsp20 molecules are slowly added to solutions already rich in pre-hydrolysed Al(III), both in terms of their amount and structural/chemical versatility, and the simultaneous interaction of more than one Al(III) entity with the same pAsp20 molecule can occur since many COOH groups per molecule are available.

This initial interaction plausibly leads to the formation of intermediate, Al(III)-rich species, which later aggregate towards final solids. Red arrows in Fig. 3(I) highlight elongated mor-

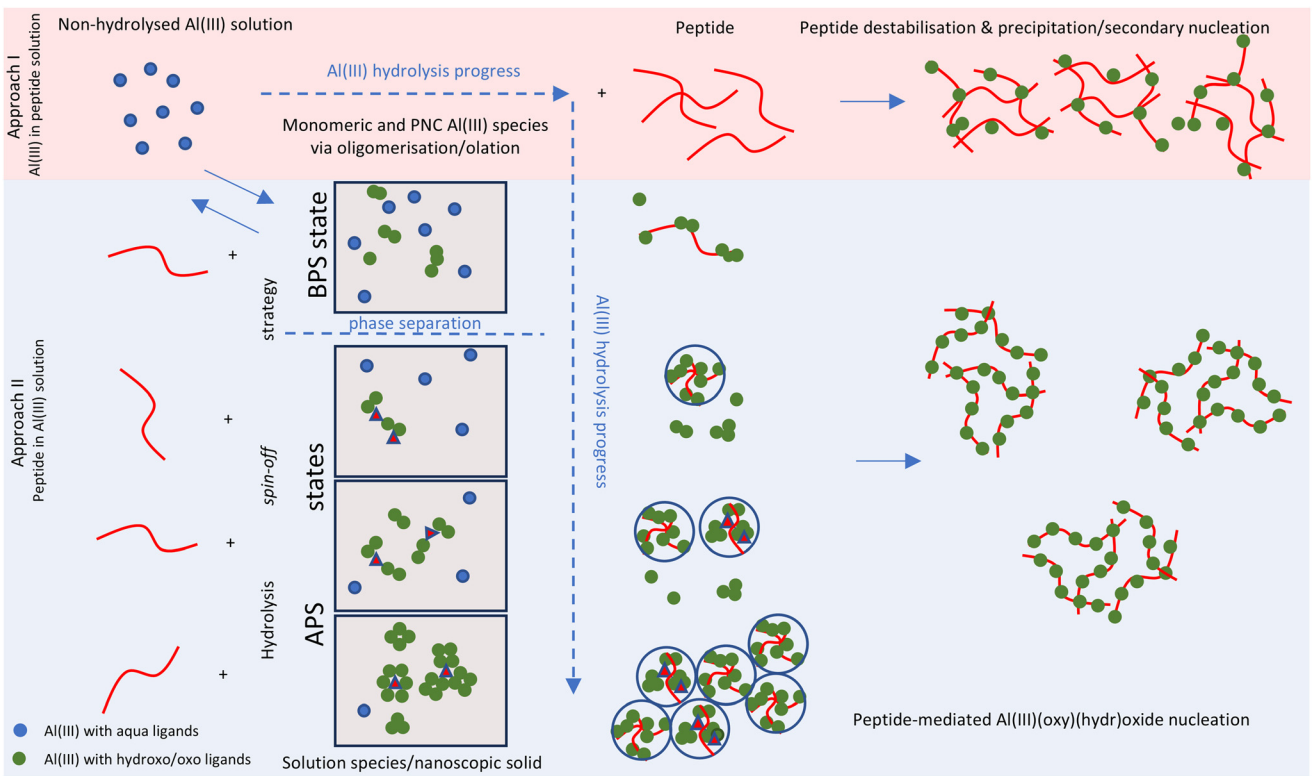

Fig. 5 Schematic illustration of the distinct investigated reaction approaches including the proposed underlying interaction mechanisms: App. I (Al(III) in peptide solution) and App. II (peptide in Al(III) solution). Solid blue circles represent undhydrolysed Al(III) with aqua ligands, solid green circles represent Al(III) with hydroxo/oxo ligands and red triangles represent tetrahedrally coordinated Al(III) species that may occur in solution after phase separation. For explanations, see the text.

phological features observed in the system following App. II, appearing between the dried blocks of the bulk material in different samples. This observation implies that the Al(III) (oxy)(hydr)oxide nucleation process could start by "mineralising" the peptide chains, but the exact nature of these features still needs to be confirmed.

The Al(III) interaction with pAsp20 cannot be considered solely as a cumulative effect of multiplied functional groups, but rather as an orchestrated response that depends on the macromolecular conformation, molecular size, hydrogen bonding, sidechain characteristics, and bond rigidity. Indeed, in neither App. I nor App. II as conducted here, metal hydrolysis and interaction of hydrolysed metal species with organic molecules occur separately, and they need to be considered as a whole, finding an optimal trade-off towards specific applications and outcomes. Although the pH level intimately influences the deprotonation degree of pAsp20, it does not significantly change in the range of pH 4 to 5, being between 40–60%,[30] and thus, cannot explain the observed experimental differences, especially as a stronger interaction would be expected at higher pH values.

Herein, we demonstrated the feasibility of a hydrolysis *"spin-off"* strategy for different Al(III) hydrolysis/phase separation states and pH values. Giving a hydrolysing system an initial chemical momentum, *i.e.*, using it for hydrolysis instead of exposing the peptide directly to highly energetic Al(III) species, leads to positive outcomes regarding the peptide-mediated formation of Al(III) (oxy)(hydr)oxide and the structural characteristics of the peptide, which are preserved to a large extent. This may be crucial in *e.g.*, pharmacy and biomedical applications. The selected hydrolysis points are often neglected in experimental procedures due to minuscule differences in the total Al(III) concentrations, accompanied by the absence of optically detectable precipitation, although they represent distinct chemical/structural states giving rise to chemically very different reaction outcomes. We speculate that controlling the initially hydrolysing system over a wide reaction window (which can comprise pH, temperature, solvent, external physical fields, spectator solute species, and any other parameter), may open new avenues towards developing hybrid inorganic–organic materials and preventing detrimental effects on vital chemical components. Eventually, this progress is based upon an improved understanding of the chemical reactions of metal hydrolytic species and the nucleation process of corresponding (oxy)(hydr)oxides.

Conclusions

We systematically studied the early stages of Al(III) (oxy)(hydr)oxide formation in the presence of a "biomimetic" model peptide poly-aspartic (pAsp20) acid using potentiometric titrations. Depending on the experimental approach, *i.e.*, adding unhydrolysed Al(III) directly into peptide solution, or adding the peptide into Al(III) solutions carefully driven to specific hydrolysis/phase separation states (with minuscule differences in the total Al(III) concentrations and no optically detectable precipitate), these two approaches resulted in distinct outcomes, Al(III)-induced peptide precipitation (alongside peptide deterioration) and peptide-mediated Al(III) (oxy)(hydr)oxide nucleation, respectively. The second experimental approach constitutes a *hydrolysis "spin-off"* strategy, allowing the controlled synthesis of hybrid materials with improved morphological homogeneity, more precisely controllable chemical and compositional characteristics, and higher thermal stability. Implementing the hydrolysis spin-off strategy proposed here can open new avenues for exploiting the rich chemistry at the mineral-organic interface, finding potential applications in environmental remediation, resource recovery and exploitation, up-cycling, medicine, and the pharmaceutical industry, requiring cost-efficient and specifically tailored chemical systems. This strategy can also be employed for plentiful organic compounds, especially those with polymeric characteristics, like peptides and proteins. Indeed, the polymer properties, such as the type of chemical bonds, the length of the sidechain, molecular mass, and structural rigidity, may influence final reaction outcomes and need to be carefully studied.

Author contributions

M. J. L. – conceptualization, data curation, formal analysis, funding, investigation, methodology, supervision, validation, visualization, writing – original draft; N. M. – data curation, formal analysis, investigation, validation; T. S. – data curation, formal analysis, investigation, validation; D. G. – conceptualization, funding, methodology, project administration, supervision, writing – review & editing.

Data availability

All data for the replication of this work are given in the ESI† file or can be obtained by the lead contact upon reasonable request.

Conflicts of interest

The authors declare no competing financial or any other interests.

Acknowledgements

This project was funded by the Deutsche Forschungsgemeinschaft (DFG, German Research Foundation) – Project number: 455689363. We thank Stella Kittel, Eduard Gross, and Katharina Nolte for their help during ICP-OES and thermal analyses. M. J. L. thanks the Ministry of Science, Technological Development and Innovation of the Republic of Serbia (Contract No: 451-03-66/2024-03/200017). The final manuscript was approved by all authors.

References

1 A. S. Cardwell, W. J. Adams, R. W. Gensemer, E. Nordheim, R. C. Santore, A. C. Ryan and W. A. Stubblefield, Chronic toxicity of aluminum, at a pH of 6, to freshwater organisms: Empirical data for the development of international regulatory standards/criteria: Aluminum freshwater chronic toxicity, *Environ. Toxicol. Chem.*, 2018, **37**, 36–48.

2 Y. Yu, J. Dong, R. Li, X. Zhao, Z. Zhu, F. Zhang, K. Zhou and X. Lin, Sodium hydrosulfide alleviates aluminum toxicity in *Brassica napus* through maintaining H_2S, ROS homeostasis and enhancing aluminum exclusion, *Sci. Total Environ.*, 2023, **858**, 160073.

3 B. Song, Q. Sun, H. Li, B. Ge, J. S. Pan, A. T. S. Wee, Y. Zhang, S. Huang, R. Zhou, X. Gao, F. Huang and H. Fang, Irreversible Denaturation of Proteins through Aluminum–Induced Formation of Backbone Ring Structures, *Angew. Chem., Int. Ed.*, 2014, **53**, 6358–6363.

4 J. I. Mujika, G. Dalla Torre, E. Formoso, R. Grande-Aztatzi, S. J. Grabowski, C. Exley and X. Lopez, Aluminum's preferential binding site in proteins: sidechain of amino acids versus backbone interactions, *J. Inorg. Biochem.*, 2018, **181**, 111–116.

5 L. Roldán-Martín, M. Sodupe and J.-D. Maréchal, Computational assessment of the impact of Cu(II) and Al (III) on β-amyloid42 fibrils: Binding sites, structural stability, and possible physiological implications, *Front. Neurosci.*, 2023, **17**, 1110311.

6 M. Turner, S. T. Mutter, O. D. Kennedy-Britten and J. A. Platts, Molecular dynamics simulation of aluminium binding to amyloid-β and its effect on peptide structure, *PLoS One*, 2019, **14**, e0217992.

7 X. T. Xu, H. W. Xu, W. Li, Y. Wang and X. Y. Zhang, A combined quantum chemical, molcular dynamics and Monto Carlo study of three amino acids as corroison inhibitors for aluminum in NaCl solution, *J. Mol. Liq.*, 2022, **345**, 117010.

8 H. Vrieling, M. Espitia Ballestas, M. Hamzink, G.-J. Willems, P. Soema, W. Jiskoot, G. Kersten and B. Metz, Stabilised aluminium phosphate nanoparticles used as vaccine adjuvant, *Colloids Surf., B*, 2019, **181**, 648–656.

9 F. A. Davila-Hernandez, B. Jin, H. Pyles, S. Zhang, Z. Wang, T. F. Huddy, A. K. Bera, A. Kang, C.-L. Chen, J. J. De Yoreo and D. Baker, Directing polymorph specific calcium carbonate formation with de novo protein templates, *Nat. Commun.*, 2023, **14**, 8191.

10 D. Qi, M. J. Lukić, H. Lu, D. Gebauer and M. Bonn, Role of Water during the Early Stages of Iron Oxyhydroxide Formation by a Bacterial Iron Nucleator, *J. Phys. Chem. Lett.*, 2024, **15**, 1048–1055.

11 O. Deschaume, K. L. Shafran and C. C. Perry, Interactions of Bovine Serum Albumin with Aluminum Polyoxocations and Aluminum Hydroxide, *Langmuir*, 2006, **22**, 10078–10088.

12 J. I. Mujika, G. D. Torre, J. I. Lachowicz and X. Lopez, In silico design of mimosine containing peptides as new efficient chelators of aluminum, *RSC Adv.*, 2019, **9**, 7688–7697.

13 Y. C. Rajan, B. S. Inbaraj and B. H. Chen, In Vitro Adsorption of Aluminum by an Edible Biopolymer Poly (γ-glutamic acid), *J. Agric. Food Chem.*, 2014, **62**, 4803–4811.

14 K. S. Lokare, N. Frank, B. Braun-Cula, I. Goikoetxea, J. Sauer and C. Limberg, Trapping Aluminum Hydroxide Clusters with Trisilanols during Speciation in Aluminum (III)–Water Systems: Reproducible, Large Scale Access to Molecular Aluminate Models, *Angew. Chem., Int. Ed.*, 2016, **55**, 12325–12329.

15 M. Piccinni, C. Rossi, D. Colombara and F. Bonaccorso, Aqueous phase synthesis and electronic spectroscopy of nanostructured layered double hydroxides, *Inorg. Chem. Front.*, 2025, **12**, 1257–1272.

16 M. J. Lukić, E. Wiedenbeck, H. Reiner and D. Gebauer, Chemical trigger toward phase separation in the aqueous Al(III) system revealed, *Sci. Adv.*, 2020, **6**, eaba6878.

17 D. Reusser, W. H. Casey and A. Navrotsky, Energetic Insight into the Formation of Solids from Aluminum Polyoxocations, *Angew. Chem., Int. Ed.*, 2015, **54**, 9253–9256.

18 Y. Tong, J. Wirth, H. Kirsch, M. Wolf, P. Saalfrank and R. K. Campen, Optically probing Al—O and O—H vibrations to characterize water adsorption and surface reconstruction on α-alumina: An experimental and theoretical study, *J. Chem. Phys.*, 2015, **142**, 054704.

19 A. Mitra, K. S. Paliwal, S. Ghosh, S. Bag, A. Roy, A. Chandrasekar and V. Mahalingam, Diaspore as an efficient halide-free catalyst for the conversion of CO2 into cyclic carbonates Inorg, *Chem. Front.*, 2023, **10**, 6329–6338.

20 P. Cárcamo-Fincheira, M. Reyes-Díaz, R. P. Omena-Garcia, A. Nunes-Nesi and C. Inostroza-Blancheteau, Physiological and metabolic responses to aluminum toxicity reveal differing resistance mechanisms to long-term exposure in highbush blueberry cultivars, *Sci. Hortic.*, 2023, **309**, 111665.

21 Y. Shan and A. Riaz, The single and interactive effects of aluminium and low pH, or Ca/Al ratios on red pine seedlings, *BMC Res. Notes*, 2023, **16**, 342.

22 D. Gebauer, M. Kellermeier, J. D. Gale, L. Bergström and H. Cölfen, Pre-nucleation clusters as solute precursors in crystallisation, *Chem. Soc. Rev.*, 2014, **43**, 2348–2371.

23 J. Scheck, B. Wu, M. Drechsler, R. Rosenberg, A. E. S. Van Driessche, T. M. Stawski and D. Gebauer, The Molecular Mechanism of Iron(III) Oxide Nucleation, *J. Phys. Chem. Lett.*, 2016, **7**, 3123–3130.

24 Z. Zheng, H. L. Nguyen, N. Hanikel, K. K.-Y. Li, Z. Zhou, T. Ma and O. M. Yaghi, High-yield, green and scalable methods for producing MOF-303 for water harvesting from desert air, *Nat. Protoc.*, 2023, **18**, 136–156.

25 K. Leetmaa, M. A. Gomez, L. Becze, F. Guo and G. P. Demopoulos, Comparative molecular characterization of aluminum hydroxy-gels derived from chloride and sulphate salts, *J. Chem. Technol. Biotechnol.*, 2014, **89**, 206–213.

26 C. Hai, L. Zhang, Y. Zhou, X. Ren, J. Liu, J. Zeng and H. Ren, Phase Transformation and Morphology Evolution

Characteristics of Hydrothermally Prepared Boehmite Particles, *J. Inorg. Organomet. Polym.*, 2018, **28**, 643–650.

27 J. Wu, F. Du, P. Zhang, I. A. Khan, J. Chen and Y. Liang, Thermodynamics of the interaction of aluminum ions with DNA: Implications for the biological function of aluminum, *J. Inorg. Biochem.*, 2005, **99**, 1145–1154.

28 L. Konermann, Addressing a Common Misconception: Ammonium Acetate as Neutral pH "Buffer" for Native Electrospray Mass Spectrometry, *J. Am. Soc. Mass Spectrom.*, 2017, **28**, 1827–1835.

29 C. Taylor, N. Schönberger, A. Laníková, M. Patzschke, B. Drobot, L. Žídek and F. Lederer, Investigation of the structure and dynamics of gallium binding to high-affinity peptides elucidated by multi-scale simulation, quantum chemistry, NMR and ITC, *Phys. Chem. Chem. Phys.*, 2021, **23**, 8618–8632.

30 M. B. Gindele, K. K. Malaszuk, C. Peter and D. Gebauer, On the Binding Mechanisms of Calcium Ions to Polycarboxylates: Effects of Molecular Weight, Side Chain, and Backbone Chemistry, *Langmuir*, 2022, **38**, 14409–14421.